Constrained Pseudoinverses for the Electromagnetic Inverse Source Problem

(Article begins on next page)

Constrained Pseudoinverses for the Electromagnetic Inverse Source Problem

Ermanno Citraro, *Graduate Student Member, IEEE*, Paolo Ricci, *Graduate Student Member, IEEE*, Alexandre Dély, Adrien Merlini, *Senior Member, IEEE*, and Francesco P. Andriulli, *Fellow, IEEE*

Abstract— Inverse source strategies have proven to be quite relevant for several applications in advanced electromagnetics. These schemes are based on the solution of ill-posed problems in which current or near-field distributions are reconstructed from far-field (or from less informative field) information. Standard strategies, that can include physical constraints such as Love conditions, often rely on standard pseudoinverse definitions and yield solutions that are, at times, far from the physical ones. This work proposes a different approach focusing on defining and analyzing a new family of pseudoinverses that takes advantage of small-in-dimension subspaces containing a priori information. The new solutions returned by the new pseudoinverses will be a suitable average between a solution living entirely in the vector space containing the a priori information and a solution obtained via norm-minimizing approaches. The contribution presents both theoretical analyses and numerical experiments showing the practical effectiveness of the novel mathematical tool.

Index Terms— A priori information, evanescent modes, integral equations, inverse source problem, Moore–Penrose (MP) pseudoinverse, vector spherical harmonics (VSH).

I. INTRODUCTION

THE electromagnetic inverse source problem, present in a variety of applications such as antenna diagnostics or antenna characterization [1], [2], requires solving an ill-posed problem [3], [4]. This ill-posedness is primarily due to the existence of nonradiating sources that can be traced back to the nontrivial solutions of the homogeneous integral equation that describes the radiation [5], [6]. This null-space, rooted in the physical and mathematical nature of the problem, is present independently of the choice of discretization; in fact, inverse approaches based either on the multipole expansion of the fields [7], [8] or on a nonorthogonal basis [9], [10], [11] all have to select a specific solution to the ill-posed problem. Several approaches have been adopted in the literature for selecting the appropriate solution. They include the choice of a specific solution norm (e.g., the popular Moore–Penrose (MP) pseudoinverse approaches, see [12] and references therein), criteria embedded in an iterative procedure [13], [14], or approaches leveraging on explicit conditions such as the Love conditions [15], [16], [17] and related [18], [19].

Moreover, the dimension of the (numerical) nullspace of the radiation matrix is further increased by the exponentially decaying contribution of the evanescent modes on the total field, when observed at far-field distances from the source. Because only a finite number of electromagnetic modes actually propagate [20], even if the presence of the null space and the consequent rank deficient matrix can be tackled via pseudoinversion, the loss of information associated with the evanescent modes is irreversible, degrades the accuracy of the solution [21], [22], and can only be handled through the injection of a priori information into the mathematical problem. This strategy has been used widely in the past to reduce the required number of samples below the Nyquist limit or, equivalently, to improve field reconstruction given a fixed number of samples (see [23], [24] and references therein). In [23], the number of samples and their position are found iteratively through the use of an orthonormal basis constructed by the simulation of the antenna under test with different design parameters. A similar construction of an overcomplete basis is presented in [24] and a given set of real samples is used to guide an iterative algorithm in the selection of the optimal subbasis. Historically, the task of finding a set of bases on which to project and approximate a given datum has also been accomplished by the compressive sampling community [25] covering a wide range of applications and integrating signal processing strategies [26].

The above-mentioned approaches are effective when the amount of information to inject is abundant enough to delineate an optimal basis to describe the observation space. Our approach will instead deal with a different scenario in which the information available is not sufficient to completely eliminate the ill-posedness of the problem, a pseudoinversion is still required, and the question of how the information at hand can be used to choose a better pseudoinversion definition with respect to a standard, a priori-information agnostic choice remains.

The purpose of this work is to propose, define, and analyze a new family of pseudoinverses that will be able to take advantage of a small-in-dimension subspace containing a priori information. The new operators can be seen as a properly chosen average between a solution living entirely in the vector space containing the a priori information and a solution obtained via a norm minimizing approach. This average is built so that the operator remains a pseudoinverse, although not of MP type. Theoretical developments are alternated with numerical studies to show the effectiveness and practical relevance of our approach when applied to real case scenarios.

The article is organized as follows. The notation and the relevant background on the inverse source problem are set in Section II. In Section III, we present a novel analysis of the radiation operator via vector spherical harmonics (VSH) basis in which the effects of the nonradiating sources and the evanescent fields on the conditioning is highlighted. The new constrained pseudoinverse is presented in Section IV while the numerical results are delineated in Section V. Finally, Section VI presents our conclusions and venues for future investigations. Very preliminary results of this article have been presented as a conference contribution [27].

II. BACKGROUND AND NOTATION

Let Ω^- be a closed domain in $\mathbb{R}^3$ with boundary Γ and complement $\Omega^+ = \mathbb{R}^3 \backslash \overline{\Omega^-}$. Consider a source located in Ω^- which radiates in $\mathbb{R}^3$ the electric and magnetic fields $\boldsymbol{E}$ and $\boldsymbol{H}$. According to the equivalence theorem, the electromagnetic problem in Ω^- can be changed (medium, fields, and sources [28]) by placing on Γ equivalent magnetic and electric current densities $\boldsymbol{M}$, $\boldsymbol{J}$ that radiate $\boldsymbol{E}$, $\boldsymbol{H}$ in Ω^+ and arbitrary new fields $\boldsymbol{E}'$, $\boldsymbol{H}'$ in Ω^-. These currents must satisfy the Maxwellian conditions at the interface

$$\boldsymbol{M} = \hat{\boldsymbol{n}} \times (\boldsymbol{E}'^- - \boldsymbol{E}^+) \tag{1}$$

$$\boldsymbol{J} = \hat{\boldsymbol{n}} \times (\boldsymbol{H}^+ - \boldsymbol{H}'^-) \tag{2}$$

where $\hat{\boldsymbol{n}}$ is the surface-normal unit vector in $\boldsymbol{r}$ directed from Ω^- to Ω^+, $\boldsymbol{E}^+$ and $\boldsymbol{H}^+$ are the original electric and magnetic fields evaluated in $\boldsymbol{r} \in \Omega^+$, and $\boldsymbol{E}'^-$ and $\boldsymbol{H}'^-$ are the new fields in $\boldsymbol{r} \in \Omega^-$. In (1) and (2), the external and internal fields are evaluated in the limit $\boldsymbol{r} \to \boldsymbol{r} \in \Gamma$ taken from Ω^+ and Ω^-, respectively. The $e^{-i\omega t}$ time dependence of the physical quantities is assumed throughout the article. The inverse source problem finds $\boldsymbol{M}$, $\boldsymbol{J}$ given field observations on a surface Γ_m in Ω^+. In this context, the electric field integral operator (EFIO) and the magnetic field integral operator (MFIO) applied to a vector function, e.g., $\boldsymbol{J}$, are defined respectively as

$$(\mathcal{T}_r \boldsymbol{J})(\boldsymbol{r}) = \hat{\boldsymbol{n}} \times \mathcal{S}_r \boldsymbol{J} = \hat{\boldsymbol{n}} \times (\mathcal{S}_{s,r} \boldsymbol{J} - \mathcal{S}_{h,r} \boldsymbol{J}) \tag{3}$$

$$(\mathcal{K}_r \boldsymbol{J})(\boldsymbol{r}) = \hat{\boldsymbol{n}} \times \mathcal{C}_r \boldsymbol{J} \tag{4}$$

where

$$(\mathcal{S}_{s,r} \boldsymbol{J})(\boldsymbol{r}) = ik \int_\Gamma g(\|\boldsymbol{r} - \boldsymbol{r}'\|) \boldsymbol{J}(\boldsymbol{r}') \, dS(\boldsymbol{r}') \tag{5}$$

$$(\mathcal{S}_{h,r} \boldsymbol{J})(\boldsymbol{r}) = \frac{1}{ik} \nabla \int_\Gamma g(\|\boldsymbol{r} - \boldsymbol{r}'\|) \nabla_s \cdot \boldsymbol{J}(\boldsymbol{r}') \, dS(\boldsymbol{r}') \tag{6}$$

$$(\mathcal{C}_r \boldsymbol{J})(\boldsymbol{r}) = \hat{\boldsymbol{n}} \times p.v. \int_\Gamma \nabla g(\|\boldsymbol{r} - \boldsymbol{r}'\|) \times \boldsymbol{J}(\boldsymbol{r}') \, dS(\boldsymbol{r}') \tag{7}$$

$\boldsymbol{r} \in \Gamma_m$ is the observation point, k is the wavenumber, and $g(\|\boldsymbol{r} - \boldsymbol{r}'\|) = (e^{ik\|\boldsymbol{r}-\boldsymbol{r}'\|}/(4\pi\|\boldsymbol{r} - \boldsymbol{r}'\|))$. If $\boldsymbol{r} \in \Gamma$, then $\mathcal{T}_r$ and $\mathcal{K}_r$ are denoted by $\mathcal{T}$ and $\mathcal{K}$, respectively. These integral operators are involved in a variety of surface and radiation electromagnetic problems. Among them, the electric field integral equation (EFIE)

$$\eta \mathcal{T} \boldsymbol{J} = -\hat{\boldsymbol{n}} \times \boldsymbol{E}^i \tag{8}$$

relates the electric current $\boldsymbol{J}$ on the surface Γ of a perfect electric conductor (PEC) to an incident electric field $\boldsymbol{E}^i$. The electromagnetic field generated by a given source in Ω^- can be evaluated in $\boldsymbol{r} \in \Gamma_m$, by means of equivalent currents as

$$\mathcal{R} \begin{bmatrix} -\boldsymbol{M} \\ \eta \boldsymbol{J} \end{bmatrix} = \begin{bmatrix} \mathcal{C}_r & \mathcal{S}_r \\ -\mathcal{S}_r & \mathcal{C}_r \end{bmatrix} \begin{bmatrix} -\boldsymbol{M} \\ \eta \boldsymbol{J} \end{bmatrix} = \begin{bmatrix} \boldsymbol{E}^+ \\ \eta \boldsymbol{H}^+ \end{bmatrix} \tag{9}$$

where $\eta = \sqrt{\mu/\epsilon}$ is the wave impedance of the considered homogeneous medium, chosen to be the same in Ω^- and Ω^+. Finally, $\hat{\boldsymbol{n}} \times \boldsymbol{E}^+$ and $\hat{\boldsymbol{n}} \times \eta \boldsymbol{H}^+$ are obtained as

$$\mathcal{R}_t \begin{bmatrix} -\boldsymbol{M} \\ \eta \boldsymbol{J} \end{bmatrix} = \begin{bmatrix} \mathcal{K}_r & \mathcal{T}_r \\ -\mathcal{T}_r & \mathcal{K}_r \end{bmatrix} \begin{bmatrix} -\boldsymbol{M} \\ \eta \boldsymbol{J} \end{bmatrix} = \begin{bmatrix} \hat{\boldsymbol{n}} \times \boldsymbol{E}^+ \\ \hat{\boldsymbol{n}} \times \eta \boldsymbol{H}^+ \end{bmatrix}. \tag{10}$$

In the following, we will consider three different discretizations of these continuous problems that are described in the three following paragraphs.

As first discretization scheme, the equivalent currents $\boldsymbol{J}$ and $\boldsymbol{M}$ are approximated with div-conforming Rao–Wilton–Glisson (RWG) basis functions $\{\boldsymbol{f}_n\}_n$ [29] defined on a triangular mesh of Γ, so that $\boldsymbol{M} \approx \sum_{n=1}^N [\boldsymbol{m}]_n \boldsymbol{f}_n$ and $\eta \boldsymbol{J} \approx \sum_{n=1}^N [\boldsymbol{j}]_n \boldsymbol{f}_n$. It is then possible to describe the fields they radiate in a homogeneous medium through

$$\mathbf{R} \begin{bmatrix} -\boldsymbol{m} \\ \boldsymbol{j} \end{bmatrix} = \begin{bmatrix} \mathbf{C}_{r,\delta} & \mathbf{S}_{r,\delta} \\ -\mathbf{S}_{r,\delta} & \mathbf{C}_{r,\delta} \end{bmatrix} \begin{bmatrix} -\boldsymbol{m} \\ \boldsymbol{j} \end{bmatrix} = \begin{bmatrix} \boldsymbol{e}_\delta \\ \boldsymbol{h}_\delta \end{bmatrix} \tag{11}$$

where $\mathbf{R}$ is the discretization of the continuous operator $\mathcal{R}$ in (9) and the elements of $\mathbf{C}_{r,\delta}$, $\mathbf{S}_{r,\delta}$ are obtained, in a point-matching fashion, as $[\mathbf{C}_{r,\delta}]_{3(m-1)+cn} = \langle \hat{\boldsymbol{u}}_c \delta(\boldsymbol{r} - \boldsymbol{r}_m), \mathcal{C}_r \boldsymbol{f}_n \rangle$ and $[\mathbf{S}_{r,\delta}]_{3(m-1)+cn} = \langle \hat{\boldsymbol{u}}_c \delta(\boldsymbol{r} - \boldsymbol{r}_m), \mathcal{S}_r \boldsymbol{f}_n \rangle$, respectively, $c \in \{1, 2, 3\}$, $\hat{\boldsymbol{u}}_c$ being the Cartesian unit vector with $\hat{\boldsymbol{u}}_1 = \hat{\boldsymbol{u}}_x$, $\hat{\boldsymbol{u}}_2 = \hat{\boldsymbol{u}}_y$, $\hat{\boldsymbol{u}}_3 = \hat{\boldsymbol{u}}_z$, $\delta(\boldsymbol{r} - \boldsymbol{r}_m)$ is the Dirac delta function centered in $\boldsymbol{r}_m$ with $\langle \hat{\boldsymbol{u}}_c \delta, \boldsymbol{f} \rangle = \int_{\mathbb{R}^3} \hat{\boldsymbol{u}}_c \delta \cdot \boldsymbol{f} \, dV$; finally, $1 \le m \le M$ with M being the number of observation points. The linear system (11) samples the electric and the magnetic field in $\boldsymbol{r}$ with $\boldsymbol{e}_\delta$ and $\boldsymbol{h}_\delta$ containing the Cartesian coordinates of the vectors $\langle \delta(\boldsymbol{r} - \boldsymbol{r}_m), \boldsymbol{E}^+ \rangle$ and $\langle \delta(\boldsymbol{r} - \boldsymbol{r}_m), \boldsymbol{H}^+ \rangle$, respectively.

An alternative to (11) can be obtained by using curl-conforming rotated RWG functions $\{\hat{\boldsymbol{n}} \times \boldsymbol{f}_n\}_n$ in place of the Dirac delta functions as test functions. The discretized boundary problem (8) then reads

$$\mathbf{T} \boldsymbol{j}^i = -\boldsymbol{e}^i \tag{12}$$

with $[\mathbf{T}]_{mn} = \langle \hat{\boldsymbol{n}} \times \boldsymbol{f}_m, \mathcal{T} \boldsymbol{f}_n \rangle$, $[\boldsymbol{e}^i]_m = \langle \hat{\boldsymbol{n}} \times \boldsymbol{f}_m, \hat{\boldsymbol{n}} \times \boldsymbol{E}^i \rangle$. Finally, the tangential fields in (10) are approximated with

$$\mathbf{R}_t \begin{bmatrix} -\boldsymbol{m} \\ \boldsymbol{j} \end{bmatrix} = \begin{bmatrix} \mathbf{K}_r & \mathbf{T}_r \\ -\mathbf{T}_r & \mathbf{K}_r \end{bmatrix} \begin{bmatrix} -\boldsymbol{m} \\ \boldsymbol{j} \end{bmatrix} = \begin{bmatrix} \boldsymbol{e} \\ \boldsymbol{h} \end{bmatrix} \tag{13}$$

where $[\mathbf{K}_r]_{mn} = \langle \hat{\boldsymbol{n}} \times \boldsymbol{f}_m, \mathcal{K}_r \boldsymbol{f}_n \rangle$, $[\mathbf{T}_r]_{mn} = \langle \hat{\boldsymbol{n}} \times \boldsymbol{f}_m, \mathcal{T}_r \boldsymbol{f}_n \rangle$, $[\boldsymbol{e}]_m = \langle \hat{\boldsymbol{n}} \times \boldsymbol{f}_m, \hat{\boldsymbol{n}} \times \boldsymbol{E}^+ \rangle$ and $[\boldsymbol{h}]_m = \langle \hat{\boldsymbol{n}} \times \boldsymbol{f}_m, \hat{\boldsymbol{n}} \times \eta \boldsymbol{H}^+ \rangle$, with $\langle \boldsymbol{f}, \boldsymbol{g} \rangle = \int_\Gamma \boldsymbol{f} \cdot \boldsymbol{g} \, dS$.

Finally, a third discretization scheme uses div-conforming Buffa–Christiansen (BC) dual basis functions $\{g_n\}_n$, defined on the dual mesh obtained through barycentric refinement of the original mesh [30] in place of the RWG basis function. In particular, the BC-discretized radiation operators $\mathbb{S}_{r,\delta}$, $\mathbb{C}_{r,\delta}$, are defined with $[\mathbb{S}_{r,\delta}]_{mn} = \langle \delta(r - r_m), \mathcal{S}_r g_n \rangle$ and $[\mathbb{C}_{r,\delta}]_{mn} = \langle \delta(r - r_m), \mathcal{C}_r g_n \rangle$. The RWG- and BC-based discretization schemes are linked through the well-conditioned change of basis matrix $\mathbb{G}_{\text{mix}}$, with $[\mathbb{G}_{\text{mix}}]_{mn} = \langle \hat{n} \times f_m, g_n \rangle$.

In the following, the different discretization strategies delineated above will be combined to form mappings between equivalent surfaces and measurement surfaces that take into account the mapping properties of the operators and the constraints in chaining the different bases.

III. SPECTRAL ANALYSIS

We present here a VSH analysis that highlights the sources of ill-posedness of (10) that describes the radiation. Consider the VSH basis [31]

$$X_{lm}(\hat{r}) = \frac{|r|}{i\sqrt{l(l+1)}}\hat{r} \times \nabla Y_{lm}(\hat{r}) \tag{14}$$

$$U_{lm}(\hat{r}) = \hat{r} \times X_{lm} \tag{15}$$

$$Y_{lm}(\hat{r}) = \hat{r} Y_{lm}(\hat{r}) \tag{16}$$

with

$$Y_{lm}(\hat{r}(\theta,\phi)) = \sqrt{\frac{(2l+1)(l-m)!}{4\pi(l+m)!}} P_{lm}(\cos\theta)e^{im\phi} \tag{17}$$

where P_{lm} are the associated Legendre polynomials and the integers l and m are such that $0 \leq l$ and $-l \leq m \leq l$. Applying (3) and (4) to a vector function expanded with (14) and (15) yields

$$\mathcal{T}_r X_{lm} = -\frac{a}{r}\mathbb{J}_l(ka)\mathbb{H}_l^{(1)}(kr)U_{lm} \tag{18}$$

$$\mathcal{T}_r U_{lm} = \frac{a}{r}\mathbb{J}_l'(ka)\mathbb{H}_l^{(1)'}(kr)X_{lm} \tag{19}$$

$$\mathcal{K}_r X_{lm} = -i\frac{a}{r}\mathbb{J}_l(ka)\mathbb{H}_l^{(1)'}(kr)X_{lm} \tag{20}$$

$$\mathcal{K}_r U_{lm} = i\frac{a}{r}\mathbb{J}_l'(ka)\mathbb{H}_l^{(1)}(kr)U_{lm} \tag{21}$$

where a is the radius of Γ, $r = \|r\|$, and $\mathbb{J}_l$, $\mathbb{H}_l^{(1)}$ are the Riccati–Bessel and the first-kind Riccati–Hankel functions, respectively. Expressions (18) to (21) are used in (10) and $\mathcal{R}_t$ is discretized with the VSH basis, truncated to $l \leq L$, as

$$\mathbf{R}_{t,\varphi} = \begin{bmatrix} \mathbf{K}_{r,\varphi} & \mathbf{T}_{r,\varphi} \\ -\mathbf{T}_{r,\varphi} & \mathbf{K}_{r,\varphi} \end{bmatrix} \tag{22}$$

where the subscript φ is used to distinguish the VSH and RWG discretizations. Then,

$$\mathbf{K}_{r,\varphi} = \begin{bmatrix} \mathbf{K}_{r,\varphi}^{XX} & \mathbf{K}_{r,\varphi}^{XU} \\ \mathbf{K}_{r,\varphi}^{UX} & \mathbf{K}_{r,\varphi}^{UU} \end{bmatrix}, \quad \mathbf{T}_{r,\varphi} = \begin{bmatrix} \mathbf{T}_{r,\varphi}^{XX} & \mathbf{T}_{r,\varphi}^{XU} \\ \mathbf{T}_{r,\varphi}^{UX} & \mathbf{T}_{r,\varphi}^{UU} \end{bmatrix}. \tag{23}$$

In (23), the superscripts XX, XU, UX, and UU denote the test and source functions couples used to discretize the associated block; for example,

$$\mathbf{K}_{r,\varphi}^{UX} = \begin{bmatrix} \langle U_{1\text{-}1}, \mathcal{K}_r X_{1\text{-}1}\rangle_\varphi & \dots & \langle U_{1\text{-}1}, \mathcal{K}_r X_{LL}\rangle_\varphi \\ \vdots & \ddots & \vdots \\ \langle U_{LL}, \mathcal{K}_r X_{1\text{-}1}\rangle_\varphi & \dots & \langle U_{LL}, \mathcal{K}_r X_{LL}\rangle_\varphi \end{bmatrix} \tag{24}$$
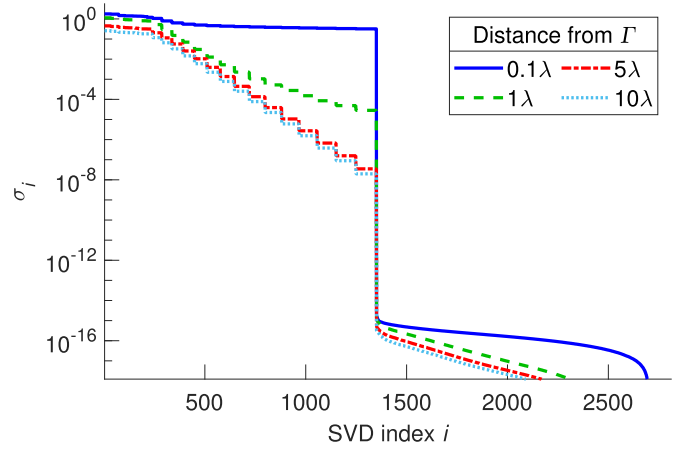

Fig. 1. Singular values of the radiation operator $\mathbf{R}_{t,\varphi}$ discretized with the VSH basis, evaluated at different distances; the σ_i are ordered with the SVD index.

where the subscripts on X_{lm}, U_{lm} span $l \leq L$, $-l \leq m \leq l$, and $\langle a, b\rangle_\varphi = 1/r^2 \int_{\Gamma_m} \overline{a} \cdot b \, dS$, for which $\langle X_{lm}, X_{l'm'}\rangle_\varphi = \delta_{ll'}\delta_{mm'}$, $\langle U_{lm}, U_{l'm'}\rangle_\varphi = \delta_{ll'}\delta_{mm'}$. Since neither $\mathbf{R}_{t,\varphi}$ nor $\mathbf{R}_{t,\varphi}^H\mathbf{R}_{t,\varphi}$ are diagonal, their singular values cannot be obtained by direct inspection. Instead, a singular value decomposition (SVD) is computed and the singular values of $\mathbf{R}_{t,\varphi}$ are shown in Fig. 1 ($a = 1$ cm, $k \approx 105$ m^{-1}, $L = 25$, $-l \leq m \leq l$). The second half of the singular values (i.e., $i > 1350$) belongs to the nullspace of the operator, while the singular values of the first half decay more rapidly as the observation distance increases [20], [21]. These singular values are associated with the evanescent fields and extend the numerical nullspace of the operator. For this reason, in practical applications, the condition number has to be limited by truncation of the singular values lower than the measurement noise floor (NF), causing an overall loss of near-field information [22].

In this work, an operator tailored for the inverse source problem uses a pseudoinverse which acts on a small subspace of a priori solutions and is able, if built properly, to recover more accurately the weakly radiating part of the solution, starting from far-field samples.

IV. NEW CONSTRAINED PSEUDOINVERSE

A. Insights and Derivation of the Proposed Pseudoinverse

First, we recall that a generic pseudoinverse $\mathbf{A}^\dagger$ of $\mathbf{A} \in \mathbb{C}^{M \times N}$ satisfies any of the properties

$$\mathbf{A}\mathbf{A}^\dagger\mathbf{A} = \mathbf{A} \quad \text{i)} \qquad \mathbf{A}^\dagger\mathbf{A}\mathbf{A}^\dagger = \mathbf{A}^\dagger \quad \text{ii)}$$

$$(\mathbf{A}\mathbf{A}^\dagger)^H = \mathbf{A}\mathbf{A}^\dagger \quad \text{iii)} \qquad (\mathbf{A}^\dagger\mathbf{A})^H = \mathbf{A}^\dagger\mathbf{A} \quad \text{iv)}$$

and the well-known MP pseudoinverse $\mathbf{A}^+$ of $\mathbf{A}$ is the unique operator which satisfies i), ii), iii), and iv). If one is only interested in finding one solution x_0 (potentially among many) of the linear system $\mathbf{A}x = b$, one can choose $x_0 = \mathbf{A}^{(1)}b$, where $\mathbf{A}^{(1)}$ is a generic pseudoinverse satisfying i) since [32]

$$\mathbf{A}x_0 = \mathbf{A}\mathbf{A}^{(1)}b = \mathbf{A}\mathbf{A}^{(1)}\mathbf{A}x = \mathbf{A}x = b. \tag{25}$$

When $\mathbf{A}^{(1)}$ varies in the set of all pseudoinverses satisfying i), denoted by $\mathbf{A}\{1\}$, $x_0 = \mathbf{A}^{(1)}b$ can be shown to deliver all possible solutions of the linear system. Since in many practical cases, there are solutions of rank-deficient matrices that have

little to no physical meaning, the condition i) alone does not ensure that the pseudoinverse and the corresponding solution have any link with the physical problem.

If we start from the opposite standpoint, we could build a pseudoinverse from existing (physical) solutions of the problem x_i, $i = 1, \ldots, P$ and the corresponding right-hand-sides $b_i = Ax_i$. By defining the matrices $\mathbf{X} \in \mathbb{C}^{N \times P}$ as $\mathbf{X}_{j,i} = [x_i]_j$ and $\mathbf{B} \in \mathbb{C}^{M \times P}$ as $\mathbf{B}_{j,i} = [b_i]_j$, we could now choose as pseudoinverse of $\mathbf{A}$ the matrix $\mathbf{XB}^\dagger$, which is a pseudoinverse of type ii) if the pseudoinverse $\mathbf{B}^\dagger$ of $\mathbf{B}$ is of type ii). This pseudoinverse provides a vector $x_0 = \mathbf{XB}^\dagger b$ which is always a linear combination of solutions of the system for selected RHSs and, if those are properly chosen, such a linear combination will exhibit physical properties. However, $\mathbf{XB}^\dagger \notin \mathbf{A}\{1\}$ unless $\mathbf{BB}^\dagger = \mathbf{I}$, i.e., this choice of pseudoinverse does not provide in general an exact solution satisfying (25). In this work, we propose a pseudoinverse that would somehow be in between the above described approaches. In particular, the pseudoinverse we propose to adopt reads

$$\mathbf{A}^\ddagger = \mathbf{A}^{(1)}(\mathbf{I} - \mathbf{BB}^\dagger) + \mathbf{XB}^\dagger \tag{26}$$

which is combining the previously defined approaches. Differently from $\mathbf{XB}^\dagger$, $\mathbf{A}^\ddagger$ provides solutions which satisfy (25) since $\mathbf{A}^\ddagger \in \mathbf{A}\{1\}$:

$$\mathbf{AA}^\ddagger\mathbf{A} = \mathbf{AA}^{(1)}(\mathbf{I} - \mathbf{BB}^\dagger)\mathbf{A} + \mathbf{AXB}^\dagger\mathbf{A} \tag{27}$$

$$= \mathbf{A} - \mathbf{AA}^{(1)}\mathbf{AXB}^\dagger\mathbf{A} + \mathbf{AXB}^\dagger\mathbf{A} \tag{28}$$

$$= \mathbf{A} \tag{29}$$

with $\mathbf{B} = \mathbf{AX}$. If $\mathbf{B}^\dagger\mathbf{B} = \mathbf{I}$, the proposed pseudoinverse yields an exact reconstruction if the RHS is entirely described by a linear combination of the columns of $\mathbf{B}$, i.e., there exists v such that $b = \mathbf{B}v$. In this case, we have

$$\mathbf{A}^\ddagger b = \mathbf{A}^{(1)}(\mathbf{B}v - \mathbf{BB}^\dagger\mathbf{B}v) + \mathbf{XB}^\dagger\mathbf{B}v \tag{30}$$

$$= \mathbf{A}^{(1)}(\mathbf{B}v - \mathbf{B}v) + \mathbf{X}v = \mathbf{X}v \tag{31}$$

where $\mathbf{X}v$ is the exact solution associated with $b = \mathbf{B}v = \mathbf{AX}v$.

B. On a Possible Strategy in Selecting Parameters for the Proposed Pseudoinverse

In the context of the inverse source problem—corresponding to $\mathbf{A} = \mathbf{R}$—the proposed pseudoinverse (26) may enhance the solution of (11) with near-field information encoded in $\mathbf{X}$. The constrained pseudoinverse (26) is flexible and can be used in different inversion contexts and applications. In particular, different inversion scenarios may lead to selecting different pseudoinverse types for $\mathbf{B}^\dagger$ and $\mathbf{R}^{(1)}$ [the latter can be of other types additionally to i)] and to different choices for the coupled matrices $\mathbf{X}$ and $\mathbf{B} = \mathbf{RX}$. In the following, we will consider the MP pseudoinverses $\mathbf{B}^+$ and $\mathbf{R}^+$ as particular choices for $\mathbf{B}^\dagger$ and $\mathbf{R}^{(1)}$, respectively.

The columns of $\mathbf{X}$ can be filled with solutions found either in real or simulated environments. In the following, we will opt for the latter. The choice of the vectors x_i is heavily dependent on the scenario. In general, however, two distinct sources that belong to the same design space up to a given perturbation of one or more of the design parameters (position and shape) will
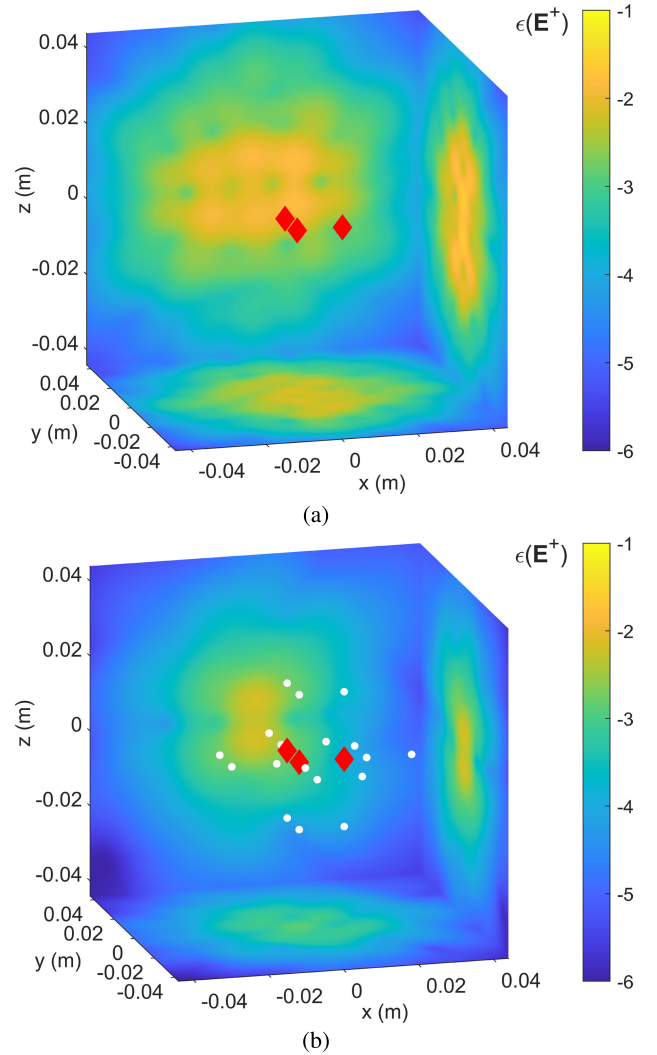

(a)

(b)

Fig. 2. Reconstruction error on a square box of side length 2.2λ centered in the origin. (a) MP reconstruction. (b) Proposed pseudoinverse $\Delta\alpha = \pi/2$. The real sources are represented with red diamonds, the constraining dipoles with white dots; the background shows $\epsilon(\mathbf{E}^+)$.

generate the same field up to a given precision. Thus, the space of a priori solutions x_i can be generated by solving several radiation problems in which these unknown parameters differ. In the following, we will provide initial application examples that will help fixing ideas.

V. NUMERICAL RESULTS

The proposed pseudoinverse is first numerically tested in a customary inverse source problem: the electric and magnetic fields generated by three electric dipoles, $\mathbf{E}^+$ and $\mathbf{H}^+$, are sampled on a finite number of points and reconstructed at arbitrary positions. The dipoles, oscillating at 5 GHz, are placed in a sphere of radius $a = 4$ cm ($\approx 0.67\lambda$) and surface Γ discretized with triangular elements of average edge length $h = \lambda/10$, where λ is the free-space wavelength. The reference magnetic and electric equivalent currents on Γ are approximated with RWG functions whose coefficients m and j are $m = -\mathbf{G}^{-1}\tilde{e}$, $j = \eta\mathbf{G}^{-1}\tilde{h}$ with $[\mathbf{G}]_{mn} = \langle f_m, f_n \rangle$, $[\tilde{e}]_m = \langle f_m, \hat{n} \times \mathbf{E}^+ \rangle$, and $[\tilde{h}]_m = \langle f_m, \hat{n} \times \mathbf{H}^+ \rangle$. The observation points on which field samples are evaluated with (11) are located on a spherical surface Γ_m, concentric to Γ, and are
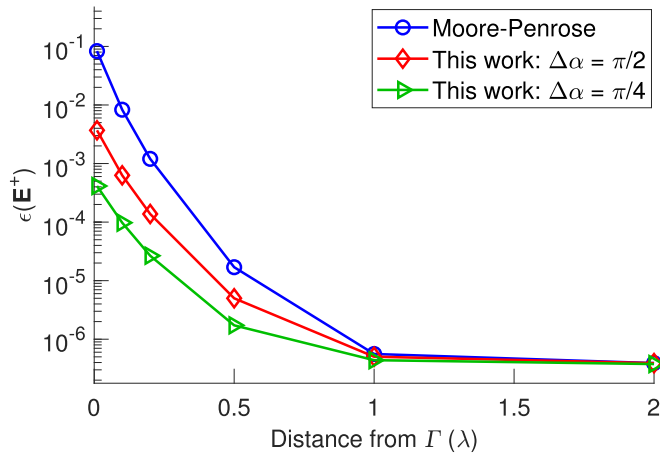
Fig. 3. Reconstruction error evaluated on spherical surfaces concentric to Γ starting from samples generated 1λ away from Γ. The MP and the proposed pseudoinverse are compared, and the latter is tested when varying the number of a priori sources (with $\Delta\alpha$) and their distance from the original source (with d). A white NF of -50 dB is applied to the far-field observations.
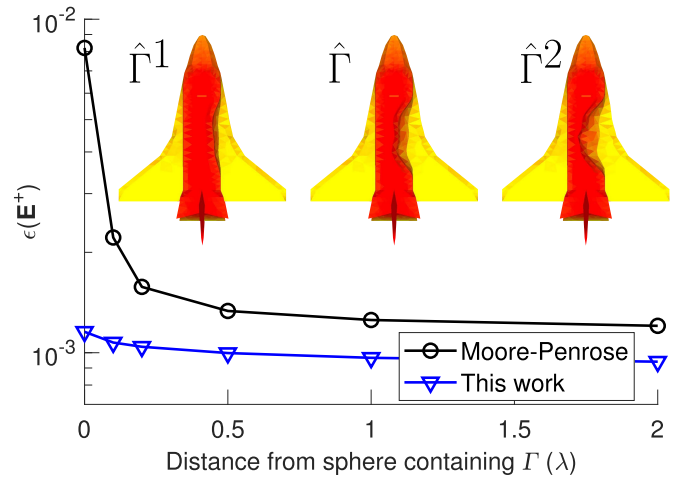

Fig. 4. Reconstruction error evaluated on concentric spherical surfaces: the MP and the proposed pseudoinverse are compared, the latter uses $\hat{\Gamma}^1$ and $\hat{\Gamma}^2$ to generate a priori vectors while the mesh of the scatterer is $\hat{\Gamma}$ (the colors of the geometries only highlight the deformations). On the x-axis, the distance 0λ coincides with the sphere of radius 8 cm enclosing Γ; the distance 1λ denotes the observation surface on which the electric field is sampled and corrupted with a Gaussian white NF of -60 dB.

distributed on uniform polar and azimuthal angle grids. The field observations are perturbed with white Gaussian noise, generating a NF of -50 dB; Γ_m is set 1λ away from Γ along its outward radial direction, and thus in a far-field region with respect to the dipole source. The injected white noise limits the reconstruction accuracy throughout all of the spatial band of radiation, in particular of the weakly radiating modes [22]. As benchmark of (26), $\mathbf{A}^{(1)}$—here chosen to be $\mathbf{A}^{(1)} = \mathbf{R}^+$ as a particular case—is regularized using a truncated-SVD. The truncation index is chosen to minimize the reconstruction error at Γ_m for the specific NF and right-hand-side under consideration. Then, a set of a priori solutions forming the columns of $\mathbf{X}$ is obtained by evaluating the equivalent currents coefficients of additional electric dipoles displaced inside Γ. These additional dipoles [the white dots in Fig. 2(b)] are displaced on spheres centered on the real sources [red diamonds in Fig. 2(b)]; the electric moment of all dipoles is identical. This test was designed to account for uncertainty in the knowledge of the position of the electromagnetic source. The goal is then to better reconstruct the fields everywhere with such a priori knowledge. The effectiveness of the choices of $\mathbf{X}, \mathbf{B}$ in (26) is investigated when varying the angular resolution $\Delta\alpha$, which controls the distance between the constraining sources (and therefore their number). Once the solution of (26) is obtained, the fields are radiated on spherical surfaces concentric to Γ, and the relative error ϵ is evaluated on each sphere as

$$\epsilon(\boldsymbol{v}) = \log_{10} \frac{\|\boldsymbol{v}_{\mathrm{ref}} - \boldsymbol{v}\|_2}{\|\boldsymbol{v}_{\mathrm{ref}}\|_2} \qquad (32)$$

where $\boldsymbol{v}$ and $\boldsymbol{v}_{\mathrm{ref}}$ are the reconstructed and reference vectors, respectively. The reconstruction errors of the new pseudoinverse (26) and of the MP pseudoinverse are shown in Fig. 3, the latter regularized through the same optimum criterion of $\mathbf{R}^+$ in (26) while keeping the same observation points; as expected, reducing $\Delta\alpha$ lowers the reconstruction error, since the dimension of the column space of $\mathbf{X}$ is increased in a meaningful way (auxiliary sources clustering around the source dipoles). We also note that at a distance of 1λ (on Γ_m), where the reconstruction points coincide with the observation points, the fields are not perfectly reconstructed and differ

slightly between the different reconstruction methods. These effects can in part be explained by numerical error propagation through ill-conditioned matrices and by the usage of different pseudoinverses. Finally, and to better appreciate the displacement of the a priori sources and the near-field reconstruction improvement, in Fig. 2, the error (32) is evaluated on a square box with edge length $2.2a$, centered at the origin: the reconstruction error for the proposed method is lower than that obtained via the MP pseudoinverse, everywhere on the sides of the box and, in particular, in the near-field regions around their centers.

The constrained pseudoinverse is now tested on a more complex scenario in which a deformed and scaled-down PEC shuttle model is illuminated by a plane wave propagating in the direction $\hat{\boldsymbol{r}} = [1, 0, 1]$ and oscillating at 5 GHz. The reference scattered field is sampled in the far-field region, and (26) is used to reconstruct more accurate scattered near-fields. The test could be representative of the case where the scatterer geometry is only approximately known and a priori assumptions can be made on the structure rather than on its displacement. First, the EFIE (12) is solved on $\hat{\Gamma}$, a triangular mesh of the shuttle illustrated in Fig. 4, and the resulting electric current is denoted by $\boldsymbol{j}^i$. Then, the equivalent magnetic and electric currents are obtained on an equivalent surface Γ wrapping the scatterer following the appropriate discretization scheme as $\boldsymbol{m} = -\mathbb{G}_{\mathrm{mix}}^{-1}\boldsymbol{e}, \boldsymbol{j} = \eta\mathbb{G}_{\mathrm{mix}}^{-1}\boldsymbol{h}$, with $\boldsymbol{e} = \mathbf{T}_r\boldsymbol{j}^i, \boldsymbol{h} = -\mathbf{K}_r\boldsymbol{j}^i$. These currents are the reference solution used to scatter the reference electric field in Ω^+, being $\mathbf{E}^+ = -\mathbb{C}_{r,\delta}\boldsymbol{m} + \mathbb{S}_{r,\delta}\boldsymbol{j}$. The constraining space of the proposed pseudoinverse makes use of two differently deformed shuttle meshes, denoted by $\hat{\Gamma}^1$ and $\hat{\Gamma}^2$ in Fig. 4. To obtain the matrix $\mathbf{X}$ of a priori solutions, the additional scatterers are illuminated with the same plane-wave applied to the reference $\hat{\Gamma}$, the corresponding EFIE are solved, and the equivalent currents are found on Γ. Thus, $\mathbf{X}$ and $\mathbf{B} = \mathbf{R}\mathbf{X}$ are composed of two columns only. Finally, the reconstruction is made on concentric spheres, the smallest just big enough to enclose Γ, starting from far-field measurements
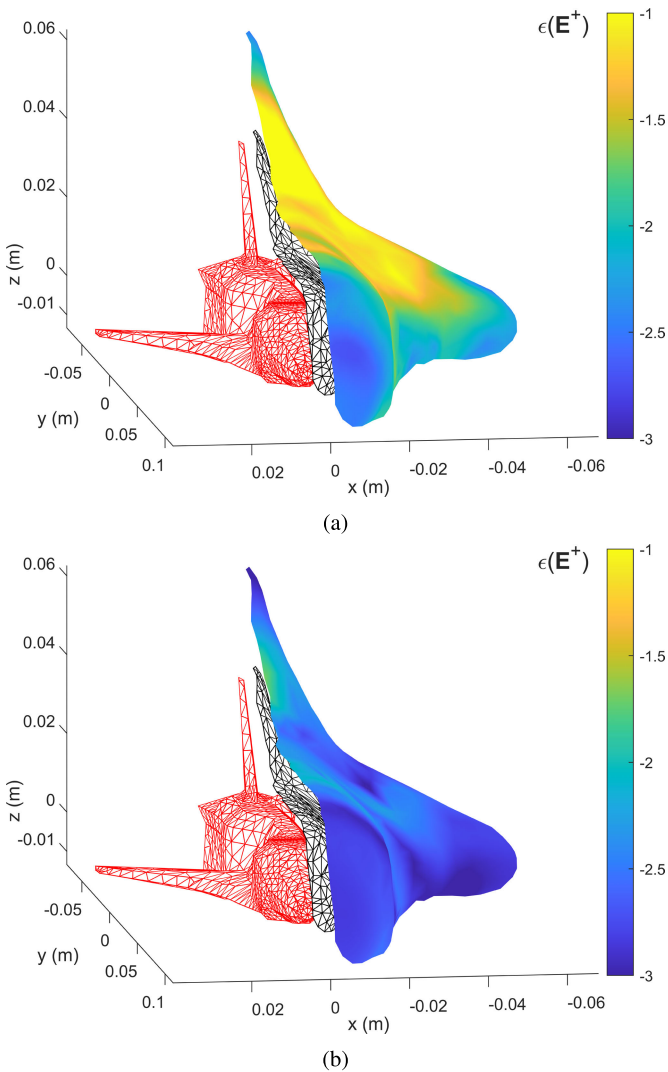
Fig. 5. Near-field reconstruction error. (a) MP reconstruction. (b) Proposed pseudoinverse given the a priori meshes of Fig. 4. The scatterer surface $\hat{\Gamma}$ is in red, the equivalent surface Γ in black and $\epsilon(\mathbf{E}^+)$ is evaluated in the near-field of Γ (distance $\approx 0.1\lambda$).

(1λ from a sphere of 8 cm radius containing Γ) corrupted with NF of -60 dB. The reconstruction error is shown in Fig. 4, where the MP pseudoinverse is compared with the constrained pseudoinverse through $\epsilon(\mathbf{E}^+)$, and there is clearly an improvement at near-field distances. Finally, in Fig. 5, $\epsilon(\mathbf{E}^+)$ is evaluated on a cut of a surface wrapping Γ at distance $\approx 0.1\lambda$; the constrained pseudoinverse yields a lower reconstruction error everywhere on the surface under consideration.

VI. CONCLUSION

This work has presented a new constrained pseudoinverse which exploits a priori information in its definition to guide the selection of a specific solution of the ill-posed inverse source problem. By its very definition, the proposed pseudoinverse should be used when a priori information is available about the source under investigation. Once this preliminary condition has been assessed, the a priori vectors can be accommodated according to a variety of strategies. We proposed and analyzed two lines of investigation: the first uses a priori information in the form of spatial knowledge of the source; the second uses a priori geometrical assumptions. In both scenarios, the proposed constrained pseudoinverse performed better than the MP pseudoinverse in reconstructing the near-fields, at the cost of generating the a priori solutions.

REFERENCES

[1] L. J. Foged, L. Scialacqua, F. Saccardi, J. L. A. Quijano, G. Vecchi, and M. Sabbadini, "Practical application of the equivalent source method as an antenna diagnostics tool [AMTA corner]," *IEEE Antennas Propag. Mag.*, vol. 54, no. 5, pp. 243–249, Oct. 2012.

[2] Y. A. Lopéz, F. L.-H. Andrés, M. R. Pino, and T. K. Sarkar, "An improved super-resolution source reconstruction method," *IEEE Trans. Instrum. Meas.*, vol. 58, no. 11, pp. 3855–3866, Nov. 2009.

[3] P. C. Hansen, "The truncated SVD as a method for regularization," *BIT Numer. Math.*, vol. 27, no. 4, pp. 534–553, Dec. 1987.

[4] A. J. Devaney, *Mathematical Foundations of Imaging, Tomography and Wavefield Inversion*. Cambridge, U.K.: Cambridge Univ. Press, 2012.

[5] E. A. Marengo and R. W. Ziolkowski, "Nonradiating and minimum energy sources and their fields: Generalized source inversion theory and applications," *IEEE Trans. Antennas Propag.*, vol. 48, no. 10, pp. 1553–1562, Oct. 2000.

[6] A. Devaney and G. Sherman, "Nonuniqueness in inverse source and scattering problems," *IEEE Trans. Antennas Propag.*, vol. AP-30, no. 5, pp. 1034–1037, Sep. 1982.

[7] E. A. Marengo and A. J. Devaney, "The inverse source problem of electromagnetics: Linear inversion formulation and minimum energy solution," *IEEE Trans. Antennas Propag.*, vol. 47, no. 2, pp. 410–412, Feb. 1999.

[8] T. F. Eibert, D. Ostrzyharczik, J. Kornprobst, and J. Knapp, "Solution of inverse source problems with distributed spherical harmonics expansions," in *Proc. 3rd URSI Atlantic Asia–Pacific Radio Sci. Meeting (AT-AP-RASC)*, May 2022, pp. 1–4.

[9] P. Petre and T. K. Sarkar, "Planar near-field to far-field transformation using an equivalent magnetic current approach," *IEEE Trans. Antennas Propag.*, vol. 40, no. 11, pp. 1348–1356, Nov. 1992.

[10] T. K. Sarkar and A. Taaghol, "Near-field to near/far-field transformation for arbitrary near-field geometry utilizing an equivalent electric current and MoM," *IEEE Trans. Antennas Propag.*, vol. 47, no. 3, pp. 566–573, Mar. 1999.

[11] O. M. Bucci and T. Isernia, "Electromagnetic inverse scattering: Retrievable information and measurement strategies," *Radio Sci.*, vol. 32, no. 6, pp. 2123–2137, Nov. 1997.

[12] E. Jørgensen, P. Meincke, C. Cappellin, and M. Sabbadini, "Improved source reconstruction technique for antenna diagnostics," in *Proc. 32nd ESA Antenna Workshop*, Sep. 2010, pp. 1–7.

[13] J. Kornprobst, R. A. M. Mauermayer, O. Neitz, J. Knapp, and T. F. Eibert, "On the solution of inverse equivalent surface-source problems," *Prog. Electromagn. Res.*, vol. 165, pp. 47–65, 2019.

[14] T. F. Eibert and C. H. Schmidt, "Multilevel fast multipole accelerated inverse equivalent current method employing Rao–Wilton–Glisson discretization of electric and magnetic surface currents," *IEEE Trans. Antennas Propag.*, vol. 57, no. 4, pp. 1178–1185, Apr. 2009.

[15] J. L. A. Quijano and G. Vecchi, "Field and source equivalence in source reconstruction on 3D surfaces," *Prog. Electromagn. Res.*, vol. 103, pp. 67–100, 2010.

[16] J. Kornprobst, R. A. Mauermayer, E. Kılıç, and T. F. Eibert, "An inverse equivalent surface current solver with zero-field enforcement by left-hand side calderón projection," in *Proc. 13th Eur. Conf. Antennas Propag. (EuCAP)*, Sep. 2019, pp. 1–3.

[17] M. Phaneuf and P. Mojabi, "On the formulation and implementation of the Love's condition constraint for the source reconstruction method," *IEEE Trans. Antennas Propag.*, vol. 70, no. 5, pp. 3613–3627, May 2022.

[18] T. F. Eibert, D. Vojvodić, and T. B. Hansen, "Fast inverse equivalent source solutions with directive sources," *IEEE Trans. Antennas Propag.*, vol. 64, no. 11, pp. 4713–4724, Nov. 2016.

[19] J. Kornprobst, J. Knapp, R. A. M. Mauermayer, O. Neitz, A. Paulus, and T. F. Eibert, "Accuracy and conditioning of surface-source based near-field to far-field transformations," *IEEE Trans. Antennas Propag.*, vol. 69, no. 8, pp. 4894–4908, Aug. 2021.

[20] E. Martini and S. Maci, "Generation of complex source point expansions from radiation integrals," *Prog. Electromagn. Res.*, vol. 152, p. 15, 2015.

[21] J. E. Hansen, *Spherical Near-Field Antenna Measurements* (IET Electromagnetic Waves Series), vol. 26, Jan. 2008.

[22] N. Mézières, M. Mattes, and B. Fuchs, "Antenna characterization from a small number of far-field measurements via reduced-order models," *IEEE Trans. Antennas Propag.*, vol. 70, no. 4, pp. 2422–2430, Apr. 2022.

[23] G. Giordanengo, M. Righero, F. Vipiana, G. Vecchi, and M. Sabbadini, "Fast antenna testing with reduced near field sampling," *IEEE Trans. Antennas Propag.*, vol. 62, no. 5, pp. 2501–2513, May 2014.

[24] M. Salucci, M. D. Migliore, G. Oliveri, and A. Massa, "Antenna measurements-by-design for antenna qualification," *IEEE Trans. Antennas Propag.*, vol. 66, no. 11, pp. 6300–6312, Nov. 2018.

[25] A. Massa, P. Rocca, and G. Oliveri, "Compressive sensing in electromagnetics—A review," *IEEE Antennas Propag. Mag.*, vol. 57, no. 1, pp. 224–238, Feb. 2015.

[26] E. J. Candes and M. B. Wakin, "An introduction to compressive sampling," *IEEE Signal Process. Mag.*, vol. 25, no. 2, pp. 21–30, Mar. 2008.

[27] E. Citraro, A. Dély, A. Merlini, and F. P. Andriulli, "On a constrained pseudoinverse for the electromagnetic inverse source problem," in *Proc. IEEE Int. Symp. Antennas Propag. USNC-URSI Radio Sci. Meeting (AP-S/URSI)*, Jul. 2022, pp. 1942–1943.

[28] R. F. Harrington, *Time-Harmonic Electromagnetic Fields*. Piscataway, NJ, USA: IEEE-Press, 2001.

[29] S. Rao, D. Wilton, and A. Glisson, "Electromagnetic scattering by surfaces of arbitrary shape," *IEEE Trans. Antennas Propag.*, vol. AP-30, no. 3, pp. 409–418, May 1982.

[30] A. Buffa and S. H. Christiansen, "A dual finite element complex on the barycentric refinement," *Comp. Rendus. Mathématique*, vol. 340, no. 6, pp. 461–464, Feb. 2005.

[31] G. C. Hsiao and R. E. Kleinman, "Mathematical foundations for error estimation in numerical solutions of integral equations in electromagnetics," *IEEE Trans. Antennas Propag.*, vol. 45, no. 3, pp. 316–328, Mar. 1997.

[32] A. Ben-Israel and T. N. E. Greville, *Generalized Inverses: Theory and Applications* (CMS Books in Mathematics), no. 15, 2nd ed., Cham, Switzerland: Springer, 2003.

Ermanno Citraro (Graduate Student Member, IEEE) received the B.Sc. and M.Sc. degrees in electrical engineering from the Politecnico di Torino, Turin, Italy, in 2017 and 2019, respectively, where he is currently pursuing the Ph.D. degree.

After a two years' working experience in the semiconductor industry, he joined the Politecnico di Torino as a Research Associate in 2021. His current research interests include computational electromagnetics, fast solvers, and brain imaging.

Mr. Citraro has authored a paper that received an honorable mention in URSI/IEEE–APS 2022.

Paolo Ricci (Graduate Student Member, IEEE) received the B.Sc. and M.Sc. degrees in computer engineering from the Politecnico di Torino, Turin, Italy, in 2018 and 2020, respectively. He is currently pursuing the Ph.D. degree in the framework of a Marie Curie EID in collaboration with the Politecnico di Torino and Thales DMS France SAS, Elancourt, France.

In 2021, he joined the Politecnico di Torino as a Research Associate. His current research interests include computational electromagnetics with a focus on integral equation formulations, fast solvers, machine learning, and applications for antenna simulations and brain imaging.

Mr. Ricci has authored a paper that received an honorable mention in URSI/IEEE–APS 2022.
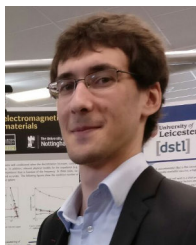
Alexandre Dély received the M.Sc.Eng. degree from the École Nationale Supérieure des Télécommunications de Bretagne (Télécom Bretagne), Brest, France, in 2015, and the Ph.D. degree from the École Nationale Supérieure Mines-Télécom Atlantique (IMT Atlantique), Brest, and the University of Nottingham, Nottingham, U.K., in 2019.

He is currently working in Thales, Elancourt, France, on electromagnetic modeling and numerical simulations. His research focuses on preconditioned and fast solution of boundary element methods frequency-domain and time-domain integral equations.
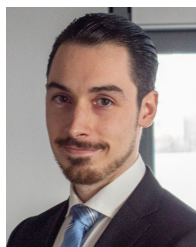
Adrien Merlini (Senior Member, IEEE) received the M.Sc.Eng. degree from the École Nationale Supérieure des Télécommunications de Bretagne (Télécom Bretagne), Brest, France, in 2015, and the Ph.D. degree from the École Nationale Supérieure Mines-Télécom Atlantique (IMT Atlantique), Brest, in 2019.

From 2018 to 2019, he was a Visiting Ph.D. student at the Politecnico di Torino, Turin, Italy, where he then joined as a Research Associate. Since 2019, he has been an Associate Professor with the Microwave Department, IMT Atlantique. His research interests include preconditioning and acceleration of integral equation solvers for electromagnetic simulations and their application in brain imaging.

Dr. Merlini is a member of IEEE-HKN, the IEEE Antennas and Propagation Society, URSI France, and the Lab-STICC laboratory. He has received two Young Scientist Awards at the URSI GASS 2020 and the EMTS 2023 meetings. In addition, he has authored a paper that won third place at EMTS 2023 and co-authored a paper that received the 2022 ICEAA-IEEE APWC Best Paper Award, five that received honorable mentions (URSI/IEEE–APS 2021, 2022, and 2023) and three Best Paper Finalists (URSI GASS 2020 and URSI/IEEE–APS 2021 and 2022). He is currently serving as an Associate Editor for *Antenna and Propagation Magazine*.

Francesco P. Andriulli (Fellow, IEEE) received the Laurea degree in electrical engineering from the Politecnico di Torino, Turin, Italy, in 2004, the M.Sc. degree in electrical engineering and computer science from the University of Illinois at Chicago, Chicago, IL, USA, in 2004, and the Ph.D. degree in electrical engineering from the University of Michigan, Ann Arbor, MI, USA, in 2008.

From 2008 to 2010, he was a Research Associate at the Politecnico di Torino. From 2010 to 2017, he was an Associate Professor (from 2010 to 2014) and then a Full Professor at the École Nationale Supérieure Mines-Télécom Atlantique (IMT Atlantique, previously ENST Bretagne), Brest, France. Since 2017, he has been a Full Professor with the Politecnico di Torino. His research interests include computational electromagnetics with focus on frequency- and time-domain integral equation solvers, well-conditioned formulations, fast solvers, low-frequency electromagnetic analyses, and modeling techniques for antennas, wireless components, microwave circuits, and biomedical applications with a special focus on brain imaging.

Prof. Andriulli is a member of Eta Kappa Nu, Tau Beta Pi, Phi Kappa Phi, and the International Union of Radio Science (URSI). He received several Best Paper Awards at conferences and symposia (URSI NA 2007, IEEE AP-S 2008, and ICEAA IEEE-APWC 2015) also in co-authorship with his students and collaborators (ICEAA IEEE-APWC 2021, EMTS 2016, URSI-DE Meeting 2014, and ICEAA 2009) with whom he also received the Second Prize Conference Paper (URSI GASS 2014), the Third Prize Conference Paper (IEEE–APS 2018), seven Honorable Mention Conference Papers (ICEAA 2011, URSI/IEEE–APS 2013, four in URSI/IEEE–APS 2022, and URSI/IEEE–APS 2023), and other three Finalist Conference Papers (URSI/IEEE-APS 2012, URSI/IEEE-APS 2007, URSI/IEEE-APS 2006, and URSI/IEEE–APS 2022). He was also a recipient of the 2014 IEEE AP-S Donald G. Dudley Jr. Undergraduate Teaching Award, the Triennium 2014–2016 URSI Issac Koga Gold Medal, and the 2015 L.B. Felsen Award for Excellence in Electrodynamics. He is the PI of the ERC Consolidator Grant: *321—From Cubic^3 To^2 Linear^1 Complexity in Computational Electromagnetics*. He served as an Associate Editor for the IEEE TRANSACTIONS ON ANTENNAS AND PROPAGATION, IEEE ANTENNAS AND WIRELESS PROPAGATION LETTERS, IEEE ACCESS, and the IET-MAP. He is an Editor-in-Chief of the *IEEE Antennas and Propagation Magazine*. He serves as a Track Editor for IEEE TRANSACTIONS ON ANTENNAS AND PROPAGATION and as an Associate Editor for *URSI Radio Science Letters*.